Stacked Sparse Autoencoder Modeling Using the Synergy of Airborne LiDAR and Satellite Optical and SAR Data to Map Forest Above-Ground Biomass

Zhenfeng Shao, Linjing Zhang, and Lei Wang

***Abstract*—Timely, spatially complete, and reliable forest above-ground biomass (AGB) data are a prerequisite to support forest management and policy formulation. Traditionally, forest AGB is spatially estimated by integrating satellite images, in particular, optical data, with field plots from forest inventory programs. However, field data are limited in remote and unmanaged areas. In addition, optical reflectance usually saturates at high-density biomass level and is subject to cloud contaminations. Thus, this study aimed to developa deep learning based workflow for mapping forest AGB by integrating Landsat 8 and Sentinel-1A images with airborne light detection and ranging (LiDAR) data. A reference AGB map was derived from the wall-to-wall LiDAR data and field measurements. The LiDAR plots—stratified random samples of forest biomass extracted from the LiDAR simulated strips in the reference map—were adopted as a surrogate for traditional field plots. In addition to the deep learning model, i.e., stacked sparse autoencoder network (SSAE), five different prediction techniques including multiple stepwise linear regressions, K-nearest neighbor, support vector machine, back propagation neural networks, and random forest were individually used to establish the relationship between LiDAR-derived forest biomass and the satellite predictors. Optical variables (Landsat 8 OLI), SAR variables (Sentinel-1A), and their combined variables were individually input to the six prediction models. Results showed that the SSAE model had the best performance forthe forest biomass estimation. The combined optical and microwave dataset as explanatory variables improved the modeling performance compared to either the optical-only or microwave-only data, regardless of prediction algorithms. The best mapping accuracy was obtained by the SSAE model with inputs of optical and microwave integrated metrics that yielded R^2 of 0.812, root mean squared error (RMSE) of 21.753 Mg/ha, and relative RMSE ($RMSE_r$) of 14.457%. Overall, the SSAE model with inputs of combined Landsat 8 OLI and Sentinel-1A information could result in accurate estimation of forest biomass by using the stratification-sampled and LiDAR-derived AGB as ground reference data. The modeling workflow has the potential to promote future forest growth monitoring and carbon stock assessment across large areas.**

***Index Terms*—Biomass, deep learning (DL), Landsat 8, light detection and ranging (LiDAR), stacked sparse autoencoder network (SSAE), Sentinel-1A.**

I. Introduction

FOREST above-ground biomass (AGB) accounting for the dominant share of terrestrial biomass stocks is a very important ecological indicator for geosciences applications [1]. Rapid and efficient mapping of forest AGB is urgently needed for the study of global climate change, especially for the assessment of above-ground carbon stocks in inaccessible areas [2]. Remote sensing has been increasingly used in estimating forest attributes due to its synoptic coverage at regional and global scales. Prediction models are typically developed to relate vegetation structure parameters with remote sensing data with the help of field samples. However, the field measurement is confronted with many challenges. On one hand, it is difficult to assess the accuracy of field data used for model calibration and validation [3]. On the other hand, it is time-consuming to collect sufficient field data covering the full range of change over large vegetated areas because vegetation growth conditions vary spatially [4]. In addition, it is impossible to collect a large amount of field data that can fully satisfy statistical sampling rules due to unpredictable forest conditions. In some circumstances, field observations require even higher costs and longer acquisition time than airborne flight data. As for remote sensing predictors, light detection and ranging (LiDAR) can provide detailed three-dimensional structure of forest canopies, and has been widely integrated with plot-based samples of forest conditions to accurately map forest attributes [5]–[7]. The commonly used LiDAR variables are height metrics which provide insights into the vertical structure of a forest stand. An increasing number of studies have demonstrated that airborne LiDAR-derived vegetation parameters, such as canopy height, canopy cover, and AGB, had reliable accuracy comparable to field measurements [2], [8], [9]. However, the airborne LiDAR data are not readily available for multitemporal applications and large-area mapping compared with frequently acquired and spatially comprehensive satellite images [10].

Manuscript received December 31, 2016; revised April 17, 2017 and June 12, 2017; accepted August 29, 2017. Date of publication September 17, 2017; date of current version December 19, 2017. This work was supported in part by the National Key Technologies Research and Development Program under Grant 2016YFB0502603, in part by the Fundamental Research Funds for the Central Universities under Grant 2042016kf0179 and Grant 2042016kf1019, in part by the Guangzhou Science and Technology Project under Grant 201604020070, in part by the National Administration of Surveying, Mapping and Geoinformation under Grant 2015NGCM, in part by the Wuhan Chen Guang Project under Grant 2016070204010114, and in part by the Special task of technical innovation in Hubei Province under Grant 2016AAA018. *(Corresponding author: Linjing Zhang.)*

The authors are with the State Key Laboratory for Information Engineering in Surveying, Mapping and Remote Sensing & Collaborative Innovation Center for Geospatial Technology, Wuhan University, Wuhan 430079, China (e-mail: shaozhenfeng@whu.edu.cn; zhanglinjing@whu.edu.cn; wlei@whu.edu.cn).

Color versions of one or more of the figures in this paper are available online at http://ieeexplore.ieee.org.

Digital Object Identifier 10.1109/JSTARS.2017.2748341

The most promising and cost-effective approach to characterize vegetation parameters at the regional or continental scale is to integrate the airborne LiDAR data with satellite data [2]. As such, sparsely sampled, LiDAR-derived vegetation parameters are used as reliable training and validation data for the satellite-based wall-to-wall mapping [2], [11]. In the study of Li *et al*. [12], sparse samples were extracted from the exhaustive LiDAR products and used in conjunction with SPOT-6 imagery to estimate forest canopy cover and biomass. Good model fits have been found between LiDAR-derived forest structural attributes and predictor variables derived from Landsat TM/ETM+ imagery, and the models have been applied to a large area using satellite images [13]. The integration of the LiDAR-derived canopy cover and height with optical variables derived from Landsat time series also resulted in satisfactory estimation performance [14].

The most common predictor metrics were optical remotely sensed data which were integrated with LiDAR-derived vegetation parameters to estimate forest canopy structure. However, optical reflectance usually reaches a saturation level during the estimation of high-density biomass [15], [16] and can be largely obscured by cloud cover and significant atmospheric aerosols. On the contrary, SAR data are immune to clouds and atmospheric aerosols and have the ability to penetrate vegetation [17]–[19]. Many radar-based estimations of forest AGB employed L-band SAR data, particularly, the Advanced Land Observing Satellite (ALOS) phased array type L-band synthetic aperture radar (PALSAR) data [20], [21] due to their strong capability to penetrate forest canopy to capture the information of the vertical structure. However, the ALOS satellite was dismissed in April 2011 and the L-band SAR data provided by the newly launched ALOS-2 satellite are costly. The successful launch of Sentinel-1A in 2014, which is equipped with a dual polarized SAR operating at C-Band (5.3 GHz), has provided a new opportunity for using radar data to estimate AGB due to its free and open data access, global coverage, short revisit intervals, and rapid product delivery. Many studies indicated significant correlations between backscattering coefficients of C-band and forest attributes such as diameter-at-breast height (DBH), volume, basal area, height, and AGB [17], [22], [23]. However, treating SAR backscattering as predictors for estimating biomass remains problematic due to not only their high sensitivity to surface roughness and soil moisture under low vegetation coverage conditions, but also to saturation at high biomass levels [24]. Considering the strengths and weaknesses of optical and SAR data and the need to overcome the restrictions associated with the employment of either data type alone, a combination of optical and SAR data has high value for AGB modeling. Actually, some promising results have also been obtained based on optical and SAR integrated information [17], [25], [26]. Limited research has been conducted to combine optical with SAR remote sensing data to estimate LiDAR-derived forest attributes.

Most studies have applied parametric approaches, such as multiple regression, to model relationships between remote sensing metrics and LiDAR-measured canopy structure [3], [27], [28]. Although frequently used and simple to interpret, parametric approaches may have difficulty in characterizing forest complexity, particularly, in areas with high structural variability [29]. Alternatively, nonparametric machine learning models have become more prevalent in recent years. As opposed to the linear regression, most of these models [e.g., K-nearest neighbor (KNN), support vector regression (SVR), back propagation neural networks (BPNN), random forest (RF), and deep learning (DL)] are sufficiently versatile to uncover complicated nonlinear relationships [30]–[32]. The KNN algorithm assigned the weighted mean of the response value from the most similar neighbor(s) to a target unit of interest, where the similarity was measured in a feature space containing candidate predictor variables [33]. Tian *et al*. [30] showed that KNN had a better performance compared to other prediction methods for forest AGB estimation. By fitting an optimal approximating hyperplane to a set of training samples, the SVR method aimed at estimating the correlation between a range of predictive variables and the target variable. The SVR has demonstrated its superiority in predicting vegetation parameters by relating spectral metrics to field samples [34], [35]. The great potential of the BPNN algorithm for estimating vegetation parameters could be attributed to the ability to find and learn complex relationships between predictor variables and vegetation parameters [36], [37]. RF was a machine learning classification and regression technique that created a great number of uncorrelated decision trees at training time and let them vote for the most accurate one. It has been successfully used in retrievals of vegetation parameters such as biomass mapping [17], [31], [38]. The DL methods have proven very effective in image classification and object detection [39]–[44]. Based on the neuroscience findings, the DL methods with multiple layers could automatically learn abstract and invariant features from the data. These automatically extracted deep features have the superior discriminatory power compared with those artificially extracted shallower features. Among the DL models, the stacked sparse autoencoder network (SSAE) has been successfully applied in image classification [44]. Additionally, limited research efforts were put to impacts of sampling strategies and comparisons between DL and other machine learning models.

The objective of this study was to integrate the LiDAR-derived AGB with the synergy of satellite optical (Landsat 8 OLI) and SAR (Sentinel-1A) data for mapping forest AGB using the DL technology for the forests in the northeast region of Conghua in the central Guangdong province, China. The wall-to-wall reference map of AGB was first derived by relating field-based biomass estimates to LiDAR-derived predictor variables. Next, stratified random sampled observations of forest biomass collected from LiDAR simulated strips in the reference map of AGB were used as a surrogate for traditional field data. Finally, relationships were separately established among forest AGB from LiDAR plots and optical variables, SAR backscattering coefficients as well as their combination using six different prediction models [SSAE, KNN, support vector machine (SVM), BPNN, RF, and multiple stepwise linear regressions (SLR)]. The best combination of the model algorithm and predictors for accurate and robust biomass estimations was identified.

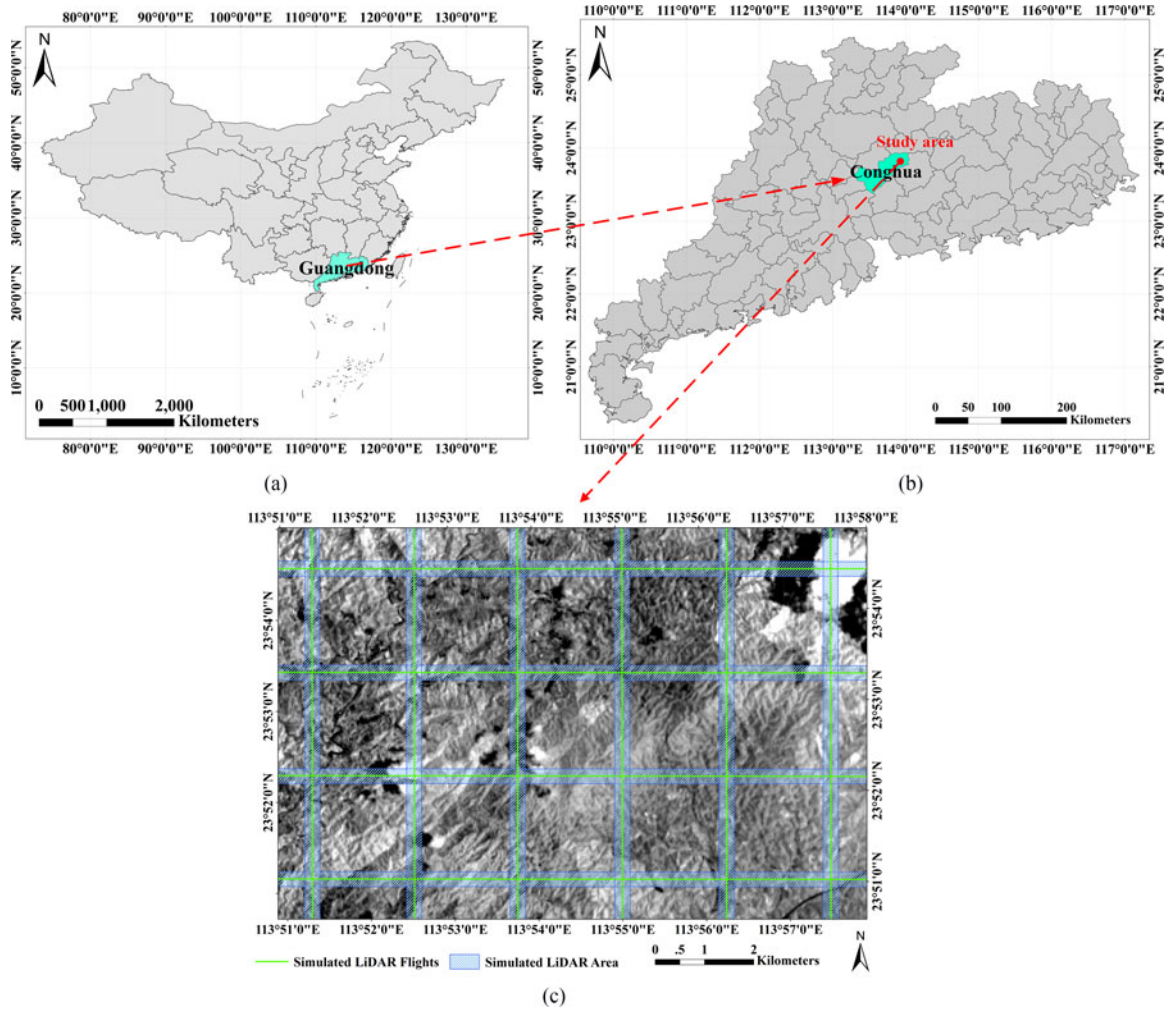

Fig. 1. Study area. (a) The location of Guangdong province in China; (b) the administrative boundary of Conghua in Guangdong province, and the location of the study area in Conghua; and (c) Landsat 8 OLI near-infrared image of the study area acquired on 1st August 2014, and the simulated LiDAR flight strips.

II. Materials

A. Study Area

This study focused on the forests area (23°52′35.65′′N, 113°54′46.17′′E, Fig. 1) located in the northeast Conghua in the central Guangdong province, China. An approximate 100 km^2 study area corresponding to the airborne LiDAR data acquisition extent ranges in elevation from 197 m in the northeast part of the area to about 621 m in the southwest. Subtropical monsoon climatic conditions prevail, with a mean annual rainfall of 1951.9 mm and mean annual temperature of approximately 21.2°C. Forested landscapes in the area are primarily coniferous and broadleaf mixed forest dominated by *Castanopsis fissa, Schima superba*, *Pinus massoniana*, and *Cinnamomum porrectum*.

B. Field Data

Field measurements were conducted in 60 field plots distributed across the study area from mid-August to the beginning of September 2013. The size of each plot was limited to 30 m $\times$ 30 m. The plot locations were determined based on subjective evaluations and almost covered the spatial extent of the LiDAR flights. Within each field plot, the tree DBH and the tree height (H) were measured using a tape and a laser hypsometer, respectively. In addition, each plot center was positioned by a GPS (Garmin MAP 60CS, accuracy $\pm$3 m) device, and species' name and type (deciduous vs. evergreen) and predominant land cover type were recorded. Trees with DBH less than 3 cm were not included in the survey. Prior to the analysis, we classified all field plots into coniferous, deciduous, and mixed forest types using a threshold of 75% [45]. If a plot was composed of more than 75% coniferous or deciduous trees, it would be labeled as coniferous or deciduous, respectively. Otherwise, the plot would be labeled as the mixed forest type [46].

In this study, we applied the method presented by Fang *et al.* [47] to estimate the AGB in each field plot. The volumes of all individual trees were first calculated using a volume table based on the DBH and H. The total volumes (TVs) in each plot were then estimated by summing up the volume of each tree. The biomass of each plot was estimated using the regression model between total AGB (TAGB) and TV [see (1)] at a megagrams

per hectare conversion unit:

$$\mathrm{TAGB} = a \times \mathrm{TV} + b \tag{1}$$

where a and b are coefficients that have been listed in [40] for different forest types. The biomass varied between 17.53 and 278.55 Mg/ha with a mean value of 110.57 Mg/ha and a standard deviation of 71.13 Mg/ha.

C. LiDAR Data Acquisition and Preprocessing

Discrete return LiDAR data for the study area were acquired under leaf-on canopy conditions in June 2013 by Urban Planning Design Survey Research Institute in Guangzhou using a fixed-wing aircraft PartenaviaP68. The LiDAR instrument was an Optech Gemini LiDAR, a two-return range detection system that recorded a maximum of two echoes per laser pulse. The sensor was set with a maximum scan angle of 15° and a pulse frequency of 70 kHz, resulting in an average density of 1.5 pulses/m^2.

Common procedures for preprocessing LiDAR data contained removal of outliers, ground/nonground classification, and normalized height computation. Preprocessing was implemented with Terrascan software (v4.006-Terrasolid, Helsinki, Finland). First, points with higher elevations than the median elevation of surrounding points and with few neighbors were removed. Subsequently, the point cloud data were separated into ground and nonground returns, and then the ground returns and all first returns were individually interpolated to form a digital elevation model (DEM) and a digital surface model (DSM) with 1 m grid cell size. The final step was to obtain a 1 m $\times$ 1 m resolution crown height model (CHM) raster layer by subtracting the DEM from the DSM. The CHM pixels with values in the range of 2–35 m were used to exclude understory vegetation and objects taller than the trees found within the region. Many studies have used 2 m to exclude nonground returns below this threshold in the calculation of LiDAR metrics [48], [49]. In this study, we found that 2 m was also an appropriate threshold for our study area on the basis of the minimum height of field-measured trees (2 m).

D. Satellite Image Acquisition and Preprocessing

The study utilized both Landsat 8 OLI and Sentinel-1A satellite images. Landsat data are among the most frequently used medium spatial-resolution data for forest AGB estimation at local and regional scales [50], [51].The Landsat 8 OLI sensor launched on the 11th of February 2013 has a 16-day temporal resolution. This sensor has two pushbroom instruments: 1) the operational land imager (OLI) consisting of nine spectral bands (see Table I), and II) the thermal infrared sensor which encompasses thermal bands 10 and 11 at a 100 m spatial resolution. Many previous studies have demonstrated that the newly launched Landsat 8 multispectral sensor has the potential to enhance AGB estimation accuracy [52], [53]. This can be attributed to the push-broom design of Landsat 8 sensor which is characterized with improved signal-to-noise ratios and high radiometric resolution of 12-bits which makes the sensor more sensitive to critical vegetation properties [54], [55]. Moreover, the refined near-infrared spectral band inhibits water vapor absorption effect at 0.825 μm and allows accurate surface spectral acquisition, which is critical in reducing sensor spectral saturation challenges. A scene of Landsat 8 image was acquired on August 2014 with a 7% of cloud coverage, sun azimuth angle of 101.26, and sun elevation angle of 66.08. The image was preprocessed using ENVI 5.1 software. The digital number was converted to top-of-atmosphere spectral radiances, following the approach described on the USGS website. The atmospheric correction of Landsat 8 OLI image to surface reflectance was subsequently implemented using the fast line-of-sight atmospheric analysis of spectral hypercube. The image was finally orthorectified using the high-resolution DEM with the projection of UTM Zone 49N/WGS-84 and RPC information.

The Sentinel-1A, carrying dual polarization SAR operating at C-band (5.3 GHz), was launched on 3 April 2014. The Sentinel-1A mission, providing free access, global coverage, short revisit intervals, and rapid product delivery, has opened up new opportunities for forest AGB estimation by using backscattering coefficients. In this study, Sentinel-1A image of the study area was acquired on August 2015. We used the level-1 interferometric wide mode ground range detected Sentinel-1A product in VV and VH polarizations. The image was acquired in ascending mode with a mean incident angle of 37.6. The Sentinel-1A image was preprocessed using the Sentinel-1 Toolbox 1.0.3. Sentinel-1A image was first radiometrically calibrated to obtain the linear radar backscattering coefficients. The SAR image was further terrain corrected using a range-Doppler terrain correction procedure with the SRTM 3Sec DEM. A single product

TABLE I
LANDSAT 8 OLI SPECTRAL AND SPATIAL CHARACTERISTICS (SOURCE: HTTP://LANDSAT.USGS.GOV)

Band	Bandwidth (λ; μm)	Spatial resolution (m)
1	0.433–0.453	30
2	0.450–0.515	30
3	0.525–0.600	30
4	0.630–0.680	30
5	0.845–0.885	30
6	1.560–1.660	30
7	2.100–2.300	30
8	0.500–0.680	15
9	1.360–1.390	30

TABLE II
LIDAR EXPLANATORY PREDICTORS

LiDAR predictors	Description
$H_{\max}$	Maximum height
H_{mean}	Mean height
H_p	10th–90th percentiles with interval of 10
H_{std}	Standard deviation of height
H_{cv}	Coefficient of height variation
H_{var}	Variance of height
H_{ske}	Height skewness
H_{kur}	Height kurtosis
Cov	Canopy cover
CRR	Canopy relief ratio

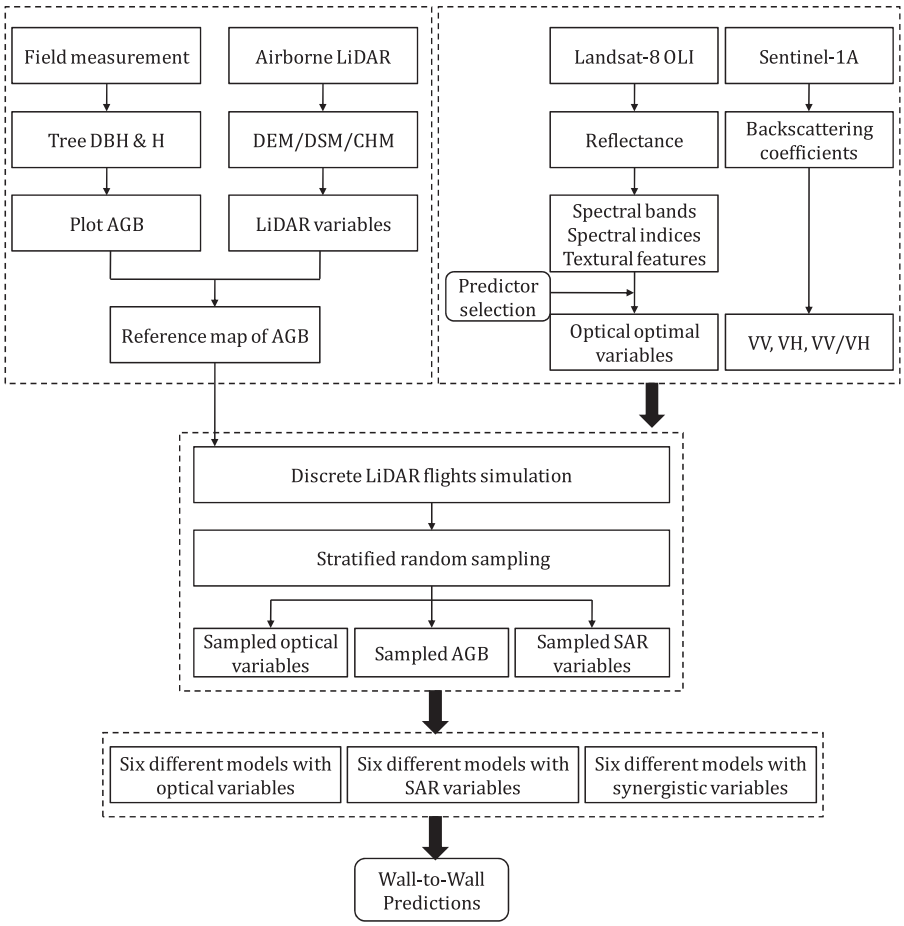

Fig. 2. Process of the modeling.

refined Lee filter with a 3 × 3 window was then used to reduce the speckle level. The image was subsequently geometrically corrected using the preprocessed Landsat 8 OLI image with an overall error of approximately 0.65 pixels. The Sentinel-1A image was resampled to the 30 m spatial resolution to be consistent with the Landsat 8 data. The last step was to resize the Landsat 8 OLI and Sentinel-1A images to accurately cover the study area.

III. Methodology

The methodology (see Fig. 2) of this study consisted of variables extraction, reference map of AGB production, stratified random sampling, and model calibration and validation. In addition, a predictor selection procedure was applied to determine the optimal variables for AGB mapping prior to the modeling.

A. Variables Extraction

1) LiDAR Metrics: We derived a total of 18 LiDAR metrics at the plot-level (see Table II). Canopy height metrics described the height distribution and dispersion of the canopy, including the maximum height ($H_{\max}$), mean height (H_{mean}), percentile height ($H_p : p_{10}, p_{20}, \ldots, p_{90}$), standard deviation of height ($\mathrm{H}_{\mathrm{std}}$), coefficient of height variation (H_{cv}), variance of height (H_{var}), skewness (H_{ske}), and kurtosis (H_{kur}). The canopy cover (Cov) was extracted to describe the fraction of canopy returns with respect to the total returns. Furthermore, a quantitative measure of the relative shape of the canopy-canopy relief ratio (CRR), describing the proportion of all returns above the mean value of heights, was calculated [56].

2) Landsat 8 OLI and Sentinel-1A Metrics: Three groups of optical metrics were calculated from the Landsat 8 OLI reflectance image: spectral bands, spectral indices, and textural features (see Table III). Extracted spectral bands contained the blue, green, red, near-infrared, SWIRI, and SWIRII (i.e., bands 2–7). Based on the published literature and the sensitivity of optical features to biomass, 11 spectral vegetation indices were calculated, including the simple ratio vegetation index (SR), normalized difference vegetation index (NDVI), enhanced vegetation index (EVI), soil adjusted vegetation index (SAVI), modified soil adjusted vegetation index (MSAVI), optimized soil-adjusted vegetation index (OSAVI), moisture stress index (MSI), green chlorophyll index (Clgreen), normalized difference water index (NDWI), atmospherically resistant vegetation index (ARVI), and green vegetation index (VIGreen). In addition, tasseled cap transformation (TCT) was a well-known linear transformation that has been widely used to characterize forest structure and conditions [57]–[59]. Five TCT components were derived based on previous studies [13], [14] (see Table III). A total of eight texture variables (i.e., mean, variance, homogeneity, contrast, dissimilarity, entropy, second moment, and

TABLE III
LANDSAT 8 OLI SPECTRAL AND TEXTURAL FEATURES USED IN THE MODELING

Type	Variable	Description
Spectral bands	Blue (B)	
	Green (G)	
	Red (R)	
	Near-infrared (NIR)	
	SWIRI	
	SWIRII	
Spectral indices	SR	Simple ratio vegetation index, $\frac{\mathrm{NIR}}{R}$
	NDVI	Normalized difference vegetation index, $\frac{\mathrm{NIR}-R}{\mathrm{NIR}+R}$
	EVI	Enhanced vegetation index, $\frac{2.5\times(\mathrm{NIR}-R)}{1+\mathrm{NIR}+6\times R-7.5\times B}$
	SAVI	Soil adjusted vegetation index, $(1+0.5)\frac{\mathrm{NIR}-R}{\mathrm{NIR}+R+0.5}$
	MSAVI	Modified soil adjusted vegetation index, $\mathrm{NIR}+0.5-\sqrt{(\mathrm{NIR}+0.5)^2-2\times(\mathrm{NIR}-R)}$
	OSAVI	Optimized soil-adjusted vegetation index, $(1+0.16)\frac{\mathrm{NIR}-R}{\mathrm{NIR}+R+0.16}$
	MSI	Moisture stress index, $\frac{\mathrm{SWIRI}}{\mathrm{NIR}}$
	Clgreen	Green chlorophyll index, $\frac{\mathrm{NIR}}{G}-1$
	NDWI	Normalized difference water index, $\frac{\mathrm{NIR}-\mathrm{SWIRI}}{\mathrm{NIR}+\mathrm{SWIRI}}$
	ARVI	Atmospherically resistant vegetation index, $\frac{\mathrm{NIR}-(2\times R-B)}{\mathrm{NIR}+(2\times R-B)}$
	VIGreen	Green vegetation index, $\frac{G-R}{G+R}$
	TCB	Tasseled cap brightness
	TCG	Tasseled cap greenness
	TCW	Tasseled cap wetness
	TCA	Tasseled cap angle, $\arctan(\mathrm{TCG}/\mathrm{TCB})$
	TCD	Tasseled cap distance, $\sqrt{(\mathrm{TCG}^2+\mathrm{TCB}^2)}$
Textural features	ME	Mean, $\sum_{i,j=0}^{N-1} iP_{i,j}$
	HO	Homogeneity, $\sum_{i,j=0}^{N-1} i\frac{P_{ij}}{1+(i-j)^2}$
	CON	Contrast, $\sum_{i,j=0}^{N-1} iP_{i,j}(i-j)^2$
	DI	Dissimilarity, $\sum_{i,j=0}^{N-1} iP_{i,j}\lvert i-j\rvert$
	EN	Entropy, $\sum_{i,j=0}^{N-1} iP_{i,j}(-\ln P_{i,j})$
	VAR	Variance, $\sum_{i,j=0}^{N-1} P_{i,j}(1-\mu_i)$
	SM	Second moment, $\sum_{i,j=0}^{N-1} iP_{i,j}{}^2$
	COR	Correlation, $\sum_{i,j=0}^{N-1} i\frac{\sum_{i,j=0}^{N-1} ijP_{i,j}-\mu_i\mu_j}{\sigma_i^2\sigma_j^2}$
$\mu_i=\sum_{i=0}^{N-1} i\sum_{j=0}^{N-1} P_{i,j};\mu_j=\sum_{j=0}^{N-1} j\sum_{j=0}^{N-1} P_{i,j};\sigma_i^2=\sum_{i=0}^{N-1}(i-\mu_i)^2\sum_{j=0}^{N-1} P_{i,j};\sigma_j^2=\sum_{j=0}^{N-1}(j-\mu_j)^2\sum_{j=0}^{N-1} P_{i,j}$		

correlation) were also extracted from the NIR image [53] using the gray level co-occurrence matrices. The full list of formula can be found in Table III. It was shown that texture measures derived from a small window size were sensitive to fine scale variations in pixel brightness when compared to those derived using large window sizes [60]. The study by Dube and Mutanga [53] found the texture measures computed from Landsat 8 OLI spectral bands using a 3×3 window size obtained the best AGB estimation accuracy compared to other window sizes. Therefore, the 3×3 window size was selected to extract the texture information using the average of four directional (horizontal, vertical, left, and right diagonal) co-occurrence matrices.

Considering the dual polarization features of the Sentinel-1A data, three radar backscatter parameters (VV, VH, VV/VH) were selected as the SAR inputs used in the tests.

B. Reference Map of AGB

The 60 plot measurements were randomly divided into training and validation datasets at a ratio of 3:1. The field-measured AGB along with LiDAR metrics (see Table II) were used to map biomass distributions using the RF algorithm.

The RF method has become popular in remote sensing as a nonlinear and nonparametric alternative, with promising

TABLE IV
PREDICTOR VARIABLES USED IN AGB ESTIMATION

Data scenarios	Data source	Details	Experiment
Optical optimal variables (OOV)	Landsat 8 OLI	Range of variable selection: spectral bands, spectral indices, and textural features (see TABLE III)	1
SAR variables (SV)	Sentinel-1A	VV, VH, VV/VH	2
OOV + SV	Landsat 8 OLI, Sentinel-1A		3

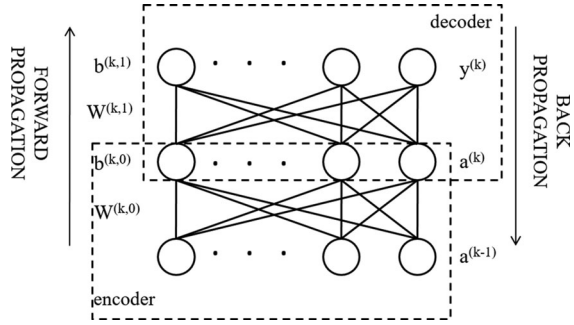

Fig. 3. Topology of the kth SAE.

predictive capabilities for high-dimensional datasets [31]. In Fassnacht *et al*. [31], the RF model achieved a satisfactory performance for the forest biomass estimation using the LiDAR data.

To improve the computational efficiency, the importance scores of all LiDAR metrics were explored to determine the optimal variables for AGB mapping. When a given variable was held out-of-bag, the percentage increase in the mean-squared error (%IncMSE) was calculated to evaluate the variable importance [61]. The larger the %IncMSE of a variable, the more important the variable. Referring to [62], we subjectively used 10% as a threshold of %IncMSE to exclude relatively poor LiDAR variables. The selected LiDAR important variables were, therefore, used for mapping the AGB distribution. A 30 m $\times$ 30 m spatially explicit LiDAR-derived AGB map was finally produced.

C. Sampling Strategy

In practice, the LiDAR data were typically available beneath discrete LiDAR flight strips rather than the wall-to-wall coverage. As such, ten discrete LiDAR flights were assumed [see Fig. 1(c)]. The north-south (NS) and east-west (EW) simulated strips in the study area were scanned with a width of 300 m. The distance interval between the strips was designed as 1800 m for both NS and EW strips according to the length/width and the forest coverage of the study area. The simulated strips covered approximately 27.78% of the entire study area.

The training and validation data were collected from the simulated LiDAR flight areas using a stratified random sampling design. Areas outside of the simulated strips were considered as unvisited or unsampled. The LiDAR height metrics H_{mean} and H_{std} were used as the prior knowledge to implement the stratification because the tree height can be treated as a direct indicator of the forest structure and growth status. After a dataset of LiDAR-derived AGB and predictor variables within the simulated strips was prepared, it was arranged in an ascending order by H_{mean} values and was then subdivided into ten equal-size strata. Subsequently, within each stratum, the subset was sorted in an ascending order by H_{std} values, and then an additional stratification into four equal-size strata was performed to produce 40 strata in total. Thereafter, 20 sampled plots were randomly selected within each stratum, which resulted in a total of 800 forest plots used as training and validation datasets at a ratio of 3:1. The number of samples for the model calibration (600) was determined according to the spatial extent of the study area (100 km^2). Similar sample sizes were used in previous studies where the spatial extent of the study area was comparable to that of our study [2], [12], [63]. The stratified random samples encompassed a comparatively large range of variability in H_{mean} and H_{std}.

D. AGB Model Calibration and Validation

1) Regression Algorithms: In our study, six different prediction models including SSAE, KNN, BPNN, SVM, RF, as well as SLR were employed to predict AGB. The SLR, a typical parametric method, was incorporated to evaluate whether the flexible and complex nonparametric models could be superior to the frequently-used SLR algorithm. The KNN, BPNN, SVM, RF, and SLR algorithms were implemented using the R statistical package [64]. SSAE was achieved using the modified DL toolbox, which is an open source library (https://github.com/rasmusbergpalm/DeepLearnToolbox#deeplearntoolbox). To the best of our knowledge, this is the first study to introduce the DL model to estimate vegetation attributes. Therefore, a detailed introduction on SSAE model is provided in the part below.

The SSAE adopted a hierarchical training strategy in establishing a deep neural network (NN) to yield deep features of data. It contained several sparse autoencoder networks (SAEs). The kth SAE is described in Fig. 3. There were two parts in the topology: an encoder and a decoder. During the forward propagation, SAE encoded the input vector $a^{(k-1)}$ into some representation $a^{(k)}$; subsequently, it reconstructed $a^{(k-1)}$ from $a^{(k)}$. In the kth SAE, the encoder mapped the input $a^{(k-1)}$ to the hidden layer to obtain the code $a^{(k)} \in R^{h^{(k)}}$ ($h^{(k}$ was the number of kth hidden units); $a^{(k)}$ was then mapped to the output layer by the decoder to acquire the reconstruction value of $a^{(k-1)}$, denoted as $y^{(k)} \in R^{h^{(k-1)}}$. The following equations [see (2) and (3)] can reveal the forward propagation of the kth SAE. The hidden layer activities of the SAE were then used as the input of the next SAE. Suppose that we have a training sample $x = (x_1, x_2, \ldots, x_d)$, $x \in R^d$, the input vector $a^{(0)} = x \in R^d$:

$$a^{(k)} = f\left(W^{(k,0)}a^{(k-1)} + b^{(k,0)}\right) \tag{2}$$

$$y^{(k)} = g\left(W^{(k,1)}a^{(k)} + b^{(k,1)}\right) \tag{3}$$

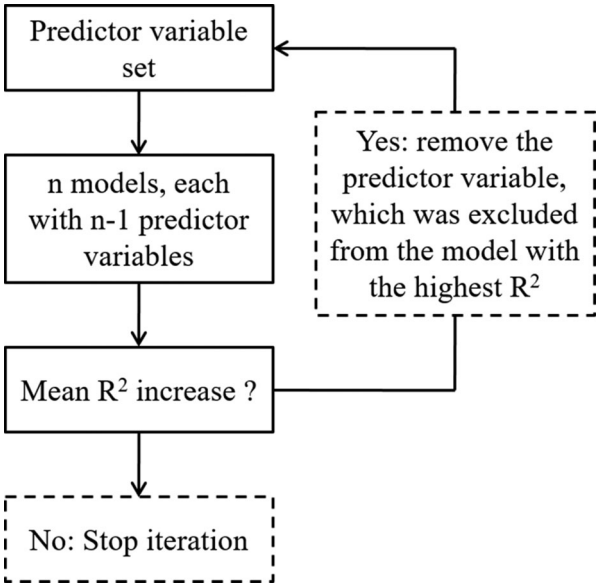

Fig. 4. Flow chart of the stepwise predictor exclusion.

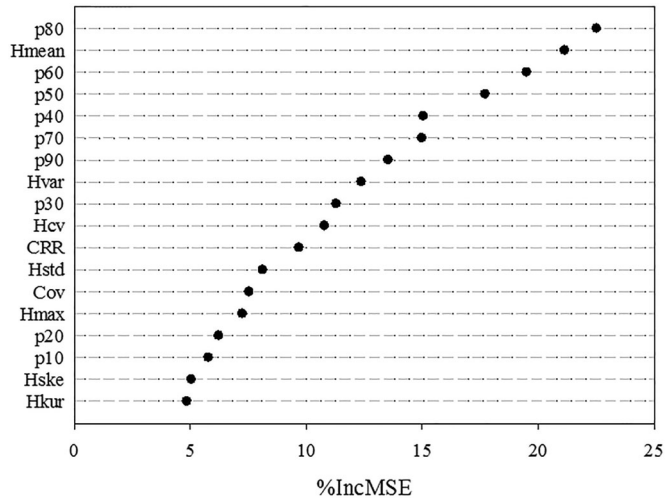

Fig. 5. Importance of LiDAR variables, denoted by the percentage increase of mean-squared error (%IncMSE) of the RF model.

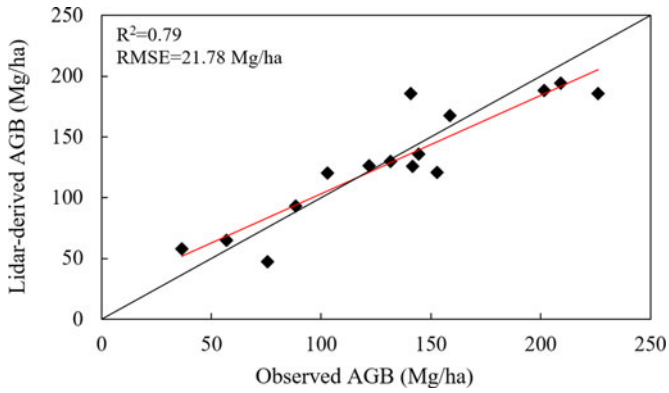

Fig. 6. Comparisons between field-measured and LiDAR-derived AGB.

where $W^{(k,0)}$, $b^{(k,0)}$ are the parameters of the encoder, and $W^{(k,1)}$, $b^{(k,1)}$ are the parameters of the decoder. $W^{(k,0)}$ is the weight matrix between the input layer and the hidden layer, and $W^{(k,1)}$ is the weight matrix between the hidden layer and the output layer. $b^{(k,0)}$ and $b^{(k,1)}$ are the bias vectors of the hidden and output layers, respectively. $a^{(k-1)}$, $a^{(k)}$, and $y^{(k)}$ are the kth input vector, the code, and the output vector, respectively. $f(\cdot)$ and $g(\cdot)$ separately denoted the activation function of hidden and output units.

When the training of each SAE was finished, the decode layers of all SAEs were removed. Because the learned features lay in the hidden layers, the encoder parameters $W^{(k,0)}$, $b^{(k,0)}$ were used to construct an SSAE in a layer-by-layer manner. Subsequently, a regression model was connected to the rear of the network to accomplish the prediction task. Therefore, the trained SAEs and the regression model were connected to build an SSAE network. To obtain a better prediction accuracy, the stochastic gradient descent algorithm [65] was applied to adjust the parameters of SSAE using the training samples. This step was called fine-tuning, which treated all layers of SSAE as a single model. The cost function J of SSAE is expressed as (5):

$$t' = \varphi(a^k) \tag{4}$$

$$J = \frac{1}{2N}\sum_{i=1}^{N} \|t_i - t_i'\|_2^2 \tag{5}$$

where $\varphi(\cdot)$ is the prediction function. t and t' are separately the true value and predicted value of the response value. N is the number of training samples.

2) Experiments: Three experiments (experiments 1–3) were conducted with different data scenarios for all the six prediction models (see Table IV). Experiments were designed as follows: Experiment 1: optimal variables selected from Landsat 8 OLI spectral bands and indices and texture features using the predictor selection method; Experiment 2: the Sentinel-1A backscatter coefficients and image-derived variables; and Experiment 3: the combined variables from experiments 1 and 2. The method for the predictor selection is detailed in Section III-E.

The results were validated using the same independent dataset ($N = 200$). Three commonly used indices were used: coefficient of determination (R^2), root mean squared error (RMSE), and relative RMSE (RMSE_r). In addition, the scatter plots and the prediction map together with the error map were also produced to globally and completely evaluate the estimation results.

E. Predictor Selection

To identify the set of predictors for the highest model performance, a stepwise procedure was used to exclude relatively poor predictors and highly intercorrelated predictors. We learned the idea of predictor selection used by Kattenborn *et al.* [66]. In each step, n models (n = number of predictors) were run using all but one predictor variable ($n - 1$). The model validation described in Section III-D2 was applied to each model. Thereby, the model which had the best performance (R^2) indirectly indicated the (excluded) predictor had the lowest explanatory power. In the next step, this predictor was removed from the set of candidate

TABLE V
ACCURACY EVALUATION FOR THE MODELS IN EXPERIMENTS 1–3 BASED ON THE VALIDATION DATASET ($N = 200$)

Experiment	Predictors	Algorithm	R^2	RMSE (Mg/ha)	$RMSE_r$ (%)
1	Optical optimal variables (OOV)	SLR	0.503	45.435	30.196
		KNN	0.558	41.643	27.676
		BPNN	0.561	40.554	26.952
		SVM	0.564	39.762	26.426
		RF	0.610	36.446	24.222
		SSAE	0.706	30.453	20.239
2	SAR variables (SV)	SLR	0.469	46.790	31.097
		KNN	0.449	48.812	32.440
		BPNN	0.462	47.770	31.748
		SVM	0.496	45.775	30.422
		RF	0.528	42.933	28.533
		SSAE	0.589	37.831	25.142
3	OOV + SV	SLR	0.594	37.482	24.910
		KNN	0.664	33.381	22.185
		BPNN	0.677	32.750	21.765
		SVM	0.684	32.127	21.352
		RF	0.744	27.995	18.606
		SSAE	0.812	21.753	14.457

predictors. Model performance was evaluated using averaged values of the different model algorithms (SLR, KNN, BPNN, SVM, RF, and SSAE). The procedure was continued until convergence of the R^2 value was reached (see Fig. 4). The stepwise procedure was used to produce optical optimal predictor variables (i.e., OOV in experiment 1).

IV. RESULTS

A. Evaluation of the Reference Map of AGB

Fig. 5 presents the importance of LiDAR variables. A variable with a higher value of %IncMSE contributes more to the predictive accuracy and is, therefore, considered to be a better variable for prediction. As can be seen from Fig. 5, the absence of p_{80}, H_{mean}, p_{60}, p_{50}, p_{40}, p_{70}, p_{90}, H_{var}, p_{30}, and H_{cv} significantly increased the %IncMSE by over 10%, indicating a decrease in the prediction accuracy of the built RF model. These LiDAR-derived metrics were, therefore, used as the prediction variables for producing the reference map of AGB.

The AGB reference map was validated against independent field measurements with R^2 of 0.79 and RMSE of 21.78 Mg/ha (see Fig. 6). This reference map showed a high accuracy comparable to or better than previous similar studies [2], [3], and provided a reliable data source for subsequent modeling. In the reference map, the biomass values ranged from 14.64 to 299.46 Mg/ha with a mean value of 115.38 Mg/ha and a standard deviation of 65.55 Mg/ha. In addition to using the data beneath the simulated LiDAR strips to perform the modeling, the wall-to-wall reference map was further used to globally evaluate the modeling results by building an error map.

B. Biomass Model Performance

The optimal optical variables selected by the stepwise selection program included: OSAVI, ARVI, SR, Clgreen, MSI, NDWI, TCA, and mean texture metric. All the three SAR backscatter parameters (VV, VH, VV/VH) were used as radar predictors because of the dual polarization characteristics of the Sentinel-1A data. All of the models were evaluated using the independent validation dataset ($N = 200$). Validation accuracies for the modeling cases in experiments 1–3 are shown in Table V. The SSAE model performed best compared to all other prediction methods, followed by the RF algorithm. The SLR model, in most cases, yielded slightly lower R^2 and higher RMSE values compared to all other algorithms. Scatter plots of the reference AGB and the estimated AGB derived from the combined optical and microwave dataset (experiment 3) showed obvious modeling differences among the six prediction algorithms (see Fig. 7). The SSAE model showed less underestimation and overestimation of biomass values compared to the other models as indicated by deviations in the slopes of the fitted trend-lines away from the 1:1 line. In addition, in experiments 1 and 2 implemented using the sole optical or SAR variables, results were always not satisfactory with $R^2 < 0.7$ and RMSE > 30 Mg/ha, regardless of the prediction methods. Furthermore, the use of optical metrics generally resulted in slightly higher R^2 and smaller RMSE values compared to that of SAR data. The differences in R^2 and RMSE between the best optical variables based model and the best SAR variables based model (prediction method: SSAE) were about 0.12 and 7.38 Mg/ha, respectively. Table V shows that the models using optical and microwave integrated dataset (i.e., OOV+ SV in experiment 3) achieved better performances compared to those with either the sole optical or microwave data, regardless of what prediction algorithm was used. As a result, the SSAE prediction algorithm with inputs of optical and SAR integrated variables produced the highest R^2 and the lowest RMSE and $RMSE_r$ values (0.812, 21.753 Mg/ha, 14.457%, respectively).

C. Wall-to-Wall Predictions

Fig. 8 illustrates the wall-to-wall biomass predictions obtained from the SSAE model of the best performance using the combined optical and microwave metrics. The predicted values

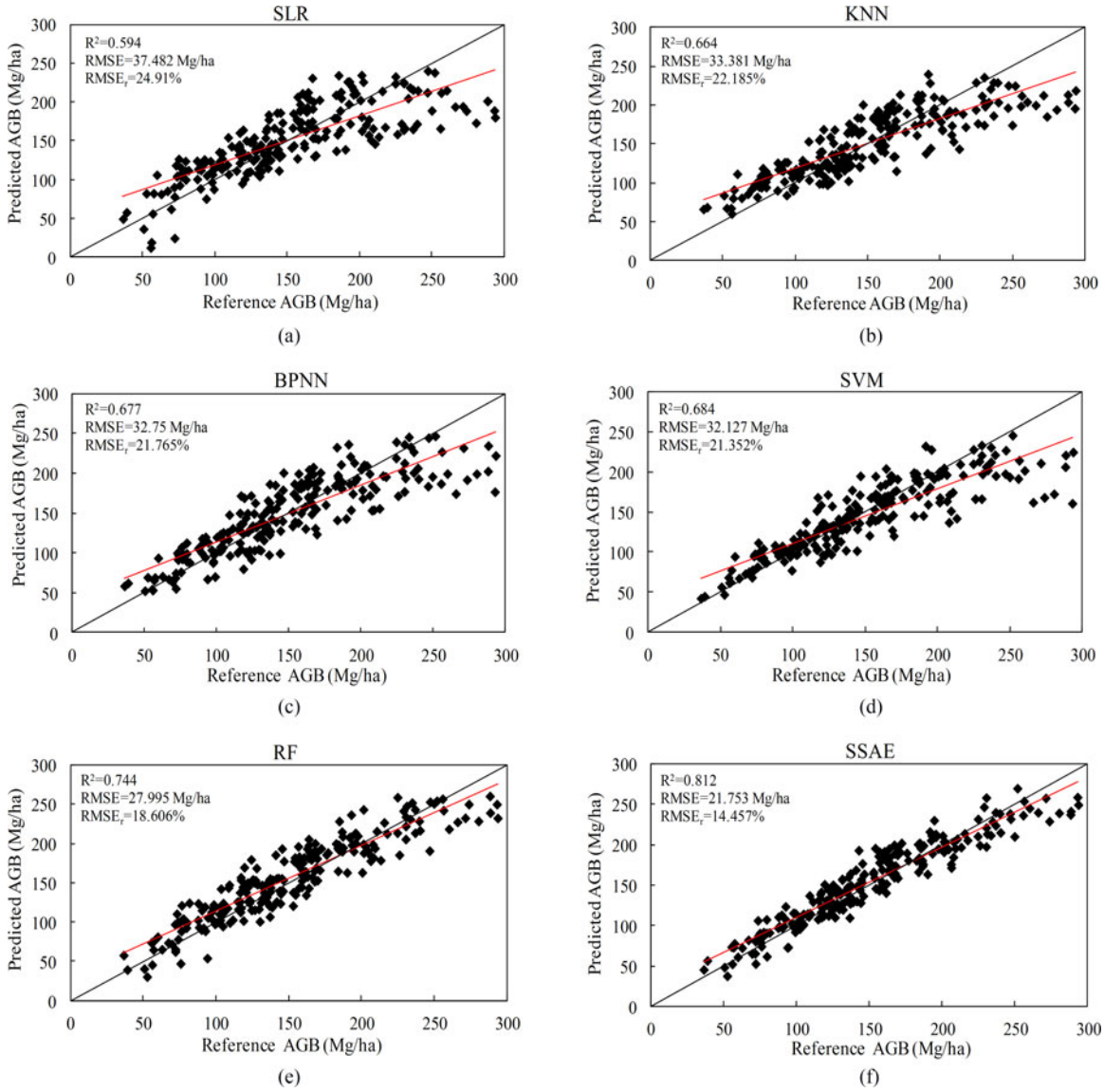

Fig. 7. Comparisons between the reference AGB and predicted AGB derived from the combined optical and SAR data (experiment 3) for the six models (SLR, KNN, BPNN, SVM, RF, and SSAE).

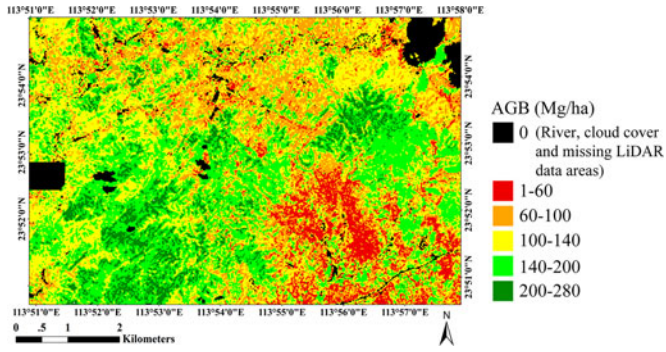

Fig. 8. Biomass map derived from the SSAE model with inputs of the combined optical and microwave metrics.

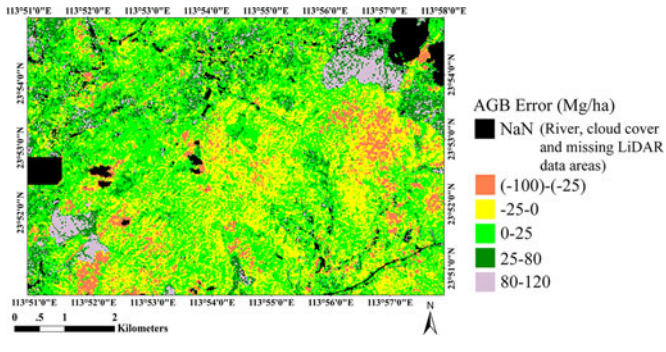

Fig. 9. Spatial distributions of estimation errors produced by the best model (SSAE model with optical and microwave integrated variables).

were in the range from 25.68 to 279.20 Mg/ha, with a mean value of 120.52 Mg/ha. The river and cloud cover areas were masked out and other nonforested areas could be identified as homogeneous areas of low predicted biomass. Fig. 9 shows the difference between the reference AGB and the predicted AGB. For most forest areas, the estimation error was less than

25 Mg/ha. It should be noted that the original LiDAR data were missing in the black rectangle located in the west of Fig. 8 (see Fig. 9) and thus this section was not taken into account during retrieving the AGB map and calculating estimation errors.

V. Discussion

A. Performances of Different Prediction Models With Different Data Inputs

Although DL models were pursued by previous studies for image classification and object detection [39]–[44], their application in estimating forest biophysical attributes was investigated for the first time. In our study, the SSAE DL model proved more efficient and superior compared to other five methods. This can be attributed to the deep architecture of SSAE in extracting much more powerful features. The input variables were mapped into another feature space, where the AGB can be accurately predicted. SSAE introduced the sparsity into its hidden layer; therefore, the overcomplete sparse features can be obtained. Besides, the representation power of DL feature can be significantly strengthened with stacked layers of NNs. The DL modeling should be considered separately for different forest types in future research, which might improve the estimation accuracy. In addition, the RF method was superior to other prediction models except the SSAE. The good predictive accuracy of RF algorithm, that was found in other studies as well [17], [31], [38], can be attributed to the regression technique of RF which differs notably from all other tested methods. Its conceptual design allows for the flexibility and robustness in regard to outliers and noise [67]. An issue in RF may be that it uses a combination of soft linear boundaries at the decision surface, thus this method may not work with small sample sizes [68]. A possible explanation for the worse performance of the SVM than the RF machine learning approaches in this study is that the irrelevant or "noise" variables may affect the building of optimal hyper-plane of SVM and decrease the accuracy of the model. Results in all the experiments suggest that SVM had better performance than BPNN and KNN, all with limited differences. Previous studies [17], [31] have demonstrated that SVM was better at solving nonlinear and high-dimensional problems compared to the BPNN and KNN. It was observed that the KNN had the worst prediction performance by using the SAR dataset. This would be related to the lack of an effective procedure to weight the prediction strength of the predictors in our implementation of KNN. In most cases, the SLR models showed evident underestimation of high values and overestimation of low values and performed worse than other models. We explain this by the fact that the relationships between the predictors and biomass are likely nonlinear and thus not well fitted by SLR.

To the best of our knowledge, the integration of the LiDAR-derived vegetation parameters with the combined optical and microwave variables in mapping forest conditions is very uncommon. The optical and microwave integrated dataset as explanatory variables improved the biomass mapping accuracy compared to either the optical-only or microwave-only data regardless of prediction algorithms. This was in accordance with earlier studies [18], [69], [70]. Attarchi and Gloaguen [26] found that the SAR and multispectral integrated variables provided the best estimation of AGB compared to either the sole optical or microwave data. In the biomass mapping, since the multispectral data are hindered by the saturation issue, the complementary use of C-band SAR data can additionally provide information related to the top canopy structure due to its penetration depth of a few centimeters [22]. In addition, the sensitivity of C-band backscatter coefficients to forest AGB can be partly attributed to heterogeneity of the forest canopy architecture [22]. Cougo *et al*. [23] suggested significant relationships between backscattering coefficients in VH, HH, and VV of C-band SAR data and the average height, DBH, and AGB. Shao and Zhang [17] found that the sensitivity of C-VH backscattering coefficients to biomass outperformed that of OSAVI when the biomass value exceeded about 100 Mg/ha. Overall, it can be concluded that the C-band SAR backscattering coefficients provide important information complementary to optical data in mapping biomass.

In the study, we first attempted to introduce the DL model to estimate forest biomass, given the superior NN of SSAE in deriving powerful deep features and its successful application in image classification. In addition, the synergy of optical and SAR data was adopted for forest biomass modeling due to the limitations associated with the use of either data type alone. The significantly improved accuracy of SSAE DL model compared to other tested prediction algorithms and the better performance of the optical and SAR integrated data in comparison with either optical-only or SAR-only data confirm the significance and value of our study. This study may be valuable in guiding further research on enhancing the estimation accuracy of forest biophysical attributes.

B. Use of LiDAR-Derived AGB as Ground Reference Data

The use of the LiDAR data as a surrogate for traditional forest inventory was rarely applied to characterize forest attributes. Although the utilization of LiDAR-derived AGB as the basic estimation data appears to be challenging, previous studies have demonstrated that this hurdle was not insurmountable [13]. Our study indicated that stratification sampling and LiDAR-derived AGB, combined with space-borne Landsat 8 OLI and Sentinel-1A data, could achieve satisfactory estimation results that were comparable to those derived from wall-to-wall LiDAR data. The modeling work was premised on the fact that the LiDAR-derived AGB was suitably reliable. The high correlation of some LiDAR metrics, such as p_{40} and p_{50}, may lead to a negative effect on the model performance of LiDAR-derived AGB. However, the importance of all the LiDAR metrics in our study (see Fig. 5) was in line with that in the similar research [62], which indicated the correctness of our variable selection routine. In addition, the good validation result of the AGB reference map (see Fig. 6) further demonstrated the effectiveness of the LiDAR variable selection method and the reliability of the LiDAR-derived AGB. Other variable selection methods should be tested in the future to improve the estimation accuracy of LiDAR-derived AGB. The modeling results can facilitate future applications of the LiDAR data as ground reference data in large-area forests where representative inventories are not available [2]. Using airborne

LiDAR data as ground reference data is likely to be a trend due to its obvious superiorities in estimating forest attributes as indicated by an increasing number of recently published studies [2], [3], [8], [63].

The attempt to use discrete LiDAR strips suggests that it is feasible to reduce the LiDAR flights during the airborne campaign, which will considerably reduce data acquisition costs. Furthermore, data reduction can significantly minimize data processing time for large-area assessments without compromising the accuracy of biomass estimates [71]. The stratified random sampling strategy utilized in our study successfully selected training and validation datasets covering the full range of AGB both statistically and geographically. Results indicated that the LiDAR metrics H_{mean} and H_{std} could be treated as effective prior knowledge in the sampling design and used for explaining changes of vegetation structures. Other LiDAR metrics, such as percentile height, can also describe the variability of vegetation structure [4], [72]. It should be noted that other sampling strategies are likely appropriate as long as samples statistically and geographically represent the entire population [63].

VI. Conclusion

Based on the modeling work in the study, we reached the following conclusions:

1) the DL model (i.e., SSAE) was explored in mapping forest AGB for the first time and produced the best estimation results compared to the other tested prediction techniques including KNN, BPNN, SVM, RF, and SLR. This improved performance of SSAE model in our study may promote the further applications of DL algorithms for estimating forest biophysical attributes.
2) The synergistic utilization of the Landsat 8 OLI and Sentinel-1A data demonstrated better performance in estimating LiDAR-derived AGB compared to either the optical-only or microwave-only data.
3) The integration of the stratification-sampled and LiDAR-derived AGB with the combined Landsat 8 OLI and Sentinel-1A information produced satisfactory biomass estimation results. This integration might show a good alternative for mapping large area biomass when the wall-to-wall LiDAR data are not available.
4) The airborne LiDAR data can be used as a prior knowledge for studies characterizing vegetation attributes in collecting effective field samples.

Overall, the SSAE model with inputs of Landsat 8 OLI and Sentinel-1A integrated variables resulted in satisfactory biomass estimation accuracy by using the LiDAR-derived AGB as ground reference data. The presented modeling workflow will greatly facilitate future forest growth monitoring and carbon stock assessments for large areas.

References

[1] R. A. Houghton, F. Hall, and S. J. Goetz, "Importance of biomass in the global carbon cycle," *J. Geophys. Res. Biogeosci.*, vol. 114, pp. 558–558, 2009.

[2] O. W. Tsui, N. C. Coops, M. A. Wulder, and P. L. Marshall, "Integrating airborne LiDAR and space-borne radar via multivariate Kriging to estimate above-ground biomass," *Remote Sens. Environ.*, vol. 139, pp. 340–352, 2013.

[3] L. Korhonen, J. Heiskanen, and I. Korpela, "Modelling Lidar-derived boreal forest canopy cover with SPOT 4 HRVIR data," *Int. J. Remote Sens.*, vol. 34, pp. 8172–8181, 2013.

[4] T. J. Hawbaker, N. S. Keuler, A. A. Lesak, G. Terje, C. Kirk, and V. C. Radeloff, "Improved estimates of forest vegetation structure and biomass with a LiDAR-optimized sampling design," *J. Geophys. Res. Atmos.*, vol. 114, pp. 363–369, 2009.

[5] H. S. J. Zald *et al.*, "Influence of Lidar, Landsat imagery, disturbance history, plot location accuracy, and plot size on accuracy of imputation maps of forest composition and structure," *Remote Sens. Environ.*, vol. 143, pp. 26–38, 2014.

[6] M. J. Falkowski, A. T. Hudak, N. L. Crookston, P. E. Gessler, E. H. Uebler, and A. M. S. Smith, "Landscape-scale parameterization of a tree-level forest growth model: a k-nearest neighbor imputation approach incorporating LiDAR data," *Can. J. Forest Res.*, vol. 40, pp. 184–199, 2010.

[7] A. T. Hudak, N. L. Crookston, J. S. Evans, D. E. Hall, and M. J. Falkowski, "Nearest neighbor imputation of species-level, plot-scale forest structure attributes from LiDAR data," *Remote Sens. Environ.*, vol. 112, pp. 2232–2245, 2008.

[8] L. Korhonen, I. Korpela, J. Heiskanen, and M. Maltamo, "Airborne discrete-return LIDAR data in the estimation of vertical canopy cover, angular canopy closure and leaf area index," *Remote Sens. Environ.*, vol. 115, pp. 1065–1080, 2011.

[9] D. Gatziolis, "Comparison of LiDAR- and photointerpretation-based estimates of canopy cover," U.S. Forest Service, Washington, DC, USA, 2012.

[10] X. Tian *et al.*, "Estimation of forest above-ground biomass using multi-parameter remote sensing data over a cold and arid area," *Int. J. Appl. Earth Obs. Geoinf.*, vol. 14, pp. 160–168, 2012.

[11] D. Stojanova, P. Panov, V. Gjorgjioski, A. Kobler, and S. Džeroski, "Estimating vegetation height and canopy cover from remotely sensed data with machine learning ☆," *Ecolgical Informat.*, vol. 5, pp. 256–266, 2010.

[12] W. Li *et al.*, "Geostatistical modeling using LiDAR-derived prior knowledge with SPOT-6 data to estimate temperate forest canopy cover and above-ground biomass via stratified random sampling," *Int. J. Appl. Earth Obs. Geoinf.*, vol. 41, pp. 88–98, 2015.

[13] H. S. J. Zald *et al.*, "Integrating Landsat pixel composites and change metrics with Lidar plots to predictively map forest structure and aboveground biomass in Saskatchewan, Canada," *Remote Sens. Environ.*, vol. 176, pp. 188–201, 2016.

[14] O. S. Ahmed, S. E. Franklin, M. A. Wulder, and J. C. White, "Characterizing stand-level forest canopy cover and height using Landsat time series, samples of airborne LiDAR, and the random forest algorithm," *ISPRS J. Photogramm. Remote Sens.*, vol. 101, pp. 89–101, 2015.

[15] S. Labrecque, R. A. Fournier, J. E. Luther, and D. Piercey, "A comparison of four methods to map biomass from Landsat-TM and inventory data in western Newfoundland," *Forest Ecology Manage.*, vol. 226, pp. 129–144, 2006.

[16] L. I. Duncanson, K. O. Niemann, and M. A. Wulder, "Integration of GLAS and Landsat TM data for aboveground biomass estimation," *Can. J. Remote Sens.*, vol. 36, pp. 129–141, 2010.

[17] Z. Shao and L. Zhang, "Estimating forest aboveground biomass by combining optical and SAR data: A case study in Genhe, Inner Mongolia, China," *Sensors*, vol. 16, 2016, Art. no. 834.

[18] S. Gao, Z. Niu, N. Huang, and X. Hou, "Estimating the Leaf Area Index, height and biomass of maize using HJ-1 and RADARSAT-2," *Int. J. Appl. Earth Obs. Geoinf.*, vol. 24, pp. 1–8, 2013.

[19] Y. Inoue *et al.*, "Season-long daily measurements of multifrequency (Ka, Ku, X, C, and L) and full-polarization backscatter signatures over paddy rice field and their relationship with biological variables," *Remote Sens. Environ.*, vol. 81, pp. 194–204, 2002.

[20] E. T. A. Mitchard *et al.*, "Measuring biomass changes due to woody encroachment and deforestation/degradation in a forest–Savanna boundary region of central Africa using multi-temporal L-band radar backscatter," *Remote Sens. Environ.*, vol. 115, pp. 2861–2873, 2011.

[21] J. M. B. Carreiras, M. J. Vasconcelos, and R. M. Lucas, "Understanding the relationship between aboveground biomass and ALOS PALSAR data in the forests of Guinea-Bissau (West Africa)," *Remote Sens. Environ.*, vol. 121, pp. 426–442, 2012.

[22] T. R. K. Chand and K. V. S. Badarinath, "Analysis of ENVISAT ASAR data for forest parameter retrieval and forest type classification - A case study over deciduous forests of central India," *Int. J. Remote Sens.*, vol. 28, pp. 4985–4999, 2007.

[23] M. Cougo *et al.*, "Radarsat-2 backscattering for the modeling of biophysical parameters of regenerating mangrove forests," *Remote Sens.*, vol. 7, pp. 17097–17112, 2015.

[24] Q. He *et al.*, "Forest stand biomass estimation using ALOS PALSAR data based on LiDAR-derived prior knowledge in the Qilian Mountain, Western China," *Int. J. Remote Sens.*, vol. 33, pp. 710–729, 2012.

[25] T. Hame, Y. Rauste, O. Antropov, and H. A. Ahola, "Improved mapping of tropical forests with optical and SAR imagery, Part II: Above ground biomass estimation," *IEEE J. Sel. Topics Appl. Earth Obs. Remote Sens.*, vol. 6, no. 1, pp. 92–101, Feb. 2013.

[26] S. Attarchi and R. Gloaguen, "Improving the estimation of above ground biomass using dual polarimetric PALSAR and ETM+ data in the Hyrcanian mountain forest (Iran)," *Remote Sens.*, vol. 6, pp. 3693–3715, 2014.

[27] M. A. Wulder and D. Seemann, "Forest inventory height update through the integration of Lidar data with segmented Landsat imagery," *Can. J. Remote Sens.*, vol. 29, pp. 536–543, 2014.

[28] T. Hilker, M. A. Wulder, and N. C. Coops, "Update of forest inventory data with Lidar and high spatial resolution satellite imagery," *Can. J. Remote Sens.*, vol. 34, pp. 5–12, 2008.

[29] G. Chen and G. J. Hay, "A support vector regression approach to estimate forest biophysical parameters at the object level using airborne Lidar transects and Quickbird data," *Photogramm. Eng. Remote Sens.*, vol. 77, pp. 733–741, 2011.

[30] X. Tian *et al.*, "Estimating Montane forest above-ground biomass in the upper reaches of the Heihe River Basin using Landsat-TM data," *Int. J. Remote Sens.*, vol. 35, pp. 7339–7362, 2014.

[31] F. E. Fassnacht *et al.*, "Importance of sample size, data type and prediction method for remote sensing-based estimations of aboveground forest biomass," *Remote Sens. Environ.*, vol. 154, pp. 102–114, 2014.

[32] B. Chen *et al.*, "Spatio-temporal prediction of leaf area index of rubber plantation using HJ-1A/1B CCD images and recurrent neural network," *ISPRS J. Photogramm. Remote Sens.*, vol. 102, pp. 148–160, 2015.

[33] H. Latifi and B. Koch, "Evaluation of most similar neighbour and random forest methods for imputing forest inventory variables using data from target and auxiliary stands," *Int. J. Remote Sens.*, vol. 33, pp. 6668–6694, 2012.

[34] J. Verrelst *et al.*, "Machine learning regression algorithms for biophysical parameter retrieval: Opportunities for Sentinel-2 and -3," *Remote Sens. Environ.*, vol. 118, pp. 127–139, 2012.

[35] D. Tuia, J. Verrelst, L. Alonso, and F. Perez-Cruz, "Multioutput support vector regression for remote sensing biophysical parameter estimation," *IEEE Geosci. Remote Sens. Lett.*, vol. 8, no. 4, pp. 804–808, Jul. 2011.

[36] S. S. Panda, D. P. Ames, and S. Panigrahi, "Application of vegetation indices for agricultural crop yield prediction using neural network techniques," *Remote Sens.*, vol. 2, pp. 673–696, 2010.

[37] K. T. Chang, L. S. Liang, F. G. Yiu, and R. Y. Wang, "Estimation of carbon sequestration by using vegetation indices," in *Proc. Geosci. Remote Sens. Symp.*, 2012, pp. 6376–6379.

[38] H. Latifi, A. Nothdurft, and B. Koch, "Non-parametric prediction and mapping of standing timber volume and biomass in a temperate forest: application of multiple optical/LiDAR-derived predictors," *Forestry*, vol. 83, pp. 395–407, 2010.

[39] Y. Yu, J. Li, H. Guan, and C. Wang, "Automated detection of three-dimensional cars in mobile laser scanning point clouds using DBM-Hough-forests," *IEEE Trans. Geosci. Remote Sens.*, vol. 57, no. 7, pp. 4130–4142, Jul. 2016.

[40] Y. Chen, Z. Lin, X. Zhao, G. Wang, and Y. Gu, "Deep learning-based classification of hyperspectral data," *IEEE J. Sel. Top. Appl. Earth Obs. Remote Sens.*, vol. 7, no. 6, pp. 2094–2107, Jun. 2014.

[41] L. Zhang, Z. Shi, and J. Wu, "A hierarchical oil tank detector with deep surrounding features for high-resolution optical satellite imagery," *IEEE J. Sel. Topics Appl. Earth Obs. Remote Sens.*, vol. 8, no. 10, pp. 4895–4909, Oct. 2015.

[42] H. Liang and Q. Li, "Hyperspectral imagery classification using sparse representations of convolutional neural network features," *Remote Sens.*, vol. 8, 2016, Art. no. 99.

[43] Y. Yu, J. Li, H. Guan, F. Jia, and C. Wang, "Learning hierarchical features for automated extraction of road markings from 3-D mobile LiDAR point clouds," *IEEE J. Sel. Topics Appl. Earth Obs. Remote Sens.*, vol. 8, no. 2, pp. 709–726, Feb. 2015.

[44] L. Zhang, W. Ma, and D. Zhang, "Stacked sparse autoencoder in PolSAR Data classification using local spatial information," *IEEE Geosci. Remote Sens. Lett.*, vol. 13, no. 9, pp. 1359–1363, Sep. 2016.

[45] K. K. Singh, G. Chen, J. B. Mccarter, and R. K. Meentemeyer, "Effects of LiDAR point density and landscape context on estimates of urban forest biomass," *ISPRS J. Photogramm. Remote Sens.*, vol. 101, pp. 310–322, 2015.

[46] C. Godwin, G. Chen, and K. K. Singh, "The impact of urban residential development patterns on forest carbon density: An integration of LiDAR, aerial photography and field mensuration," *Landscape Urban Plan.*, vol. 136, pp. 97–109, 2015.

[47] J. Fang, G. Liu, and S. Xu, "Biomass and net production of forest vegetation in China," *Acta Ecologica Sinica*, vol. 16, pp. 497–508, 1996.

[48] J. Hyyppa *et al.*, "Advances in forest inventory using airborne laser scanning," *Remote Sens.*, vol. 4, pp. 1190–1207, 2012.

[49] M. A. Wulder *et al.*, "Lidar sampling for large-area forest characterization: A review," *Remote Sens. Environ.*, vol. 121, pp. 196–209, 2012.

[50] D. Lu, "The potential and challenge of remote sensing-based biomass estimation," *Int. J. Remote Sens.*, vol. 27, pp. 1297–1328, 2006.

[51] C. J. Gleason and J. H. Im, "A review of remote sensing of forest biomass and biofuel: Options for small-area applications," *Geosci. Remote Sens.*, vol. 48, pp. 141–170, 2011.

[52] T. Dube, O. Mutanga, T. Dube, and O. Mutanga, "Evaluating the utility of the medium-spatial resolution Landsat 8 multispectral sensor in quantifying aboveground biomass in uMgeni catchment, South Africa," *ISPRS J. Photogramm. Remote Sens.*, vol. 101, pp. 36–46, 2015.

[53] T. Dube and O. Mutanga, "Investigating the robustness of the new Landsat-8 operational land imager derived texture metrics in estimating plantation forest aboveground biomass in resource constrained areas," *ISPRS J. Photogramm. Remote Sens.*, vol. 108, pp. 12–32, 2015.

[54] H. El-Askary, S. H. A. El-Mawla, J. Li, M. M. El-Hattab, and M. El-Raey, "Change detection of coral reef habitat using Landsat-5 TM, Landsat 7 ETM+ and Landsat 8 OLI data in the Red Sea (Hurghada, Egypt)," *Int. J. Remote Sens.*, vol. 35, pp. 2327–2346, 2014.

[55] N. Pahlevan and J. R. Schott, "Leveraging EO-1 to evaluate capability of new generation of Landsat sensors for coastal/inland water studies," *IEEE J. Sel. Topics Appl. Earth Obs. Remote Sens.*, vol. 6, no. 2, pp. 360–374, Apr. 2013.

[56] G. Chirici, R. E. Mcroberts, L. Fattorini, M. Mura, and M. Marchetti, "Comparing echo-based and canopy height model-based metrics for enhancing estimation of forest aboveground biomass in a model-assisted framework," *Remote Sens. Environ.*, vol. 174, pp. 1–9, 2016.

[57] S. P. Healey, Z. Yang, W. B. Cohen, and D. J. Pierce, "Application of two regression-based methods to estimate the effects of partial harvest on forest structure using Landsat data," *Remote Sens. Environ.*, vol. 101, pp. 115–126, 2006.

[58] W. B. Cohen, T. A. Spies, R. J. Alig, D. R. Oetter, T. K. Maiersperger, and M. Fiorella, "Characterizing 23 Years (1972–95) of stand replacement disturbance in western Oregon forests with Landsat imagery," *Ecosystems*, vol. 5, pp. 122–137, 2002.

[59] M. A. Wulder, J. C. White, B. Bentz, M. F. Alvarez, and N. C. Coops, "Estimating the probability of mountain pine beetle red-attack damage," *Remote Sens. Environ.*, vol. 101, pp. 150–166, 2006.

[60] K. Kelsey and J. Neff, "Estimates of aboveground biomass from texture analysis of Landsat imagery," *Remote Sens.*, vol. 6, pp. 6407–6422, 2014.

[61] Y. Su *et al.*, "Spatial distribution of forest aboveground biomass in China: Estimation through combination of spaceborne Lidar, optical imagery, and forest inventory data," *Remote Sens. Environ.*, vol. 173, pp. 187–199, 2016.

[62] M. Li, J. Im, L. J. Quackenbush, and T. Liu, "Forest biomass and carbon stock quantification using airborne LiDAR data: A case study over Huntington wildlife forest in the Adirondack park," *IEEE J. Sel. Topics Appl. Earth Obs. Remote Sens.*, vol. 7, no. 7, pp. 3143–3156, Jul. 2014.

[63] A. T. Hudak, M. A. Lefsky, W. B. Cohen, and M. Berterretche, "Integration of Lidar and Landsat ETM+ data for estimating and mapping forest canopy height," *Remote Sens. Environ.*, vol. 82, pp. 397–416, 2002.

[64] C. R. Team, "Team RDC.R: A language and environment for statistical computing. R Foundation for statistical computing: Vienna, Austria," *Computing*, vol. 1, pp. 12–21, 2013.

[65] O. Bousquet, U. V. Luxburg, and G. Rätsch, "*Advanced Lectures on Machine Learning* (Lecture Notes in Computer Science), vol. 3176. New York, NY, USA: Springer, 2004.

[66] T. Kattenborn, J. Maack, F. Faßnacht, F. Enßle, J. Ermert, and B. Koch, "Mapping forest biomass from space – Fusion of hyperspectral EO1-hyperion data and Tandem-X and WorldView-2 canopy height models," *Int. J. Appl. Earth Obs. Geoinf.*, vol. 35, pp. 359–367, 2015.

[67] L. Breiman, "Random forests," *Mach. Learn.*, vol. 45, pp. 5–32, 2001.
[68] P. Krahwinkler and J. Rossman, "Using decision tree based multiclass support vector machines for forest mapping," in *Proc. IEEE Int. Geosci. Remote Sens. Symp.*, Vancouver, Canada, 2011, pp. 949–952.
[69] S. Deng, M. Katoh, Q. Guan, N. Yin, and M. Li, "Estimating forest aboveground biomass by combining ALOS PALSAR and WorldView-2 data: A case study at Purple Mountain National Park, Nanjing, China," *Remote Sens.*, vol. 6, pp. 7878–7910, 2014.
[70] T. M. Basuki, A. Skidmore, Y. Hussin, and I. Van Duren, "Estimating tropical forest biomass more accurately by integrating ALOS PALSAR and Landsat-7 ETM+ data," *Int. J. Remote Sens.*, vol. 34, pp. 4871–4888, 2013.
[71] K. K. Singh, G. Chen, J. B. Vogler, and R. K. Meentemeyer, "When big data are too much: Effects of LiDAR Returns and point density on estimation of forest biomass," *IEEE J. Sel. Topics Appl. Earth Obs. Remote Sens.*, vol. 9, no. 7, pp. 3210–3218, Jul. 2016.
[72] E. Næsset, "Predicting forest stand characteristics with airborne scanning laser using a practical two-stage procedure and field data," *Remote Sens. Environ.*, vol. 80, pp. 88–99, 2002.

Zhenfeng Shao received the Ph.D. degree in aerial photogrammetry from Wuhan University, Wuhan, China, in 2004.

He is currently a Professor in the State Key Laboratory of Information Engineering in Surveying, Mapping and Remote Sensing, Wuhan University. His research interests include remote sensing and environment monitoring.

Linjing Zhang is currently working toward the Ph.D. degree in the State Key Laboratory of Information Engineering in Surveying, Mapping and Remote Sensing, Wuhan University, Wuhan, China.

Her research interests include forest parameters estimation and ecological environment remote sensing.

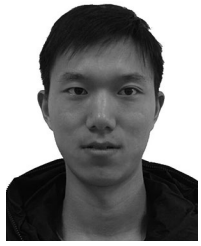

Lei Wang is currently working toward the Ph.D. degree in photogrammetry and remote sensing at Wuhan University, Wuhan, China.

His research interests include 3-D point cloud processing, computer vision, and 3-D modeling.